Short-pulse inversion of inhomogeneous media: a time-domain diffraction tomography

Timor Melamed, Yael Ehrlich and Ehud Heyman

Tel-Aviv University, Faculty of Engineering, Department of Electrical Engineering—Physical Electronics, Tel-Aviv 69978, Israel

Abstract. Time-domain inversion of a three-dimensional inhomogeneous medium is formulated as a time-domain diffraction tomography. The scattered data are expanded into a spectrum of time-dependent plane waves using the slant-stack transform. It is then shown that each time-dependent plane-wave constituent in the data is directly related to the Radon transform of the medium's inhomogeneity along the direction that bisects the angle between the plane wave and the incident wave. This new tomographic relation provides the basis for two inversion approaches: a Radon-space reconstruction and a time-dependent filtered backpropagation. Finally, the reconstruction errors due to the limited spacetime aperture are identified via analysis and a numerical example.

1. Introduction

Inversion of an inhomogeneous medium is in general a nonlinear problem. Direct solutions exist only for a few special configurations, hence this problem is usually addressed by iterative schemes (e.g. [1–3]) or by linearized models (e.g. [4–8]). This work is concerned with a three-dimensional short-pulse linearized inversion using a new time-domain diffraction tomography formulation. Since the main goal in this work is to explore the new time-domain operations, the theory is formulated here within the weak scattering Born approximation, but it may readily be extended to the Rytov approximation.

Diffraction tomography involves processing of data from multiple independent experiments. Typical configurations involve a single frequency with multiple source locations, or multiple frequencies with a fixed source configuration. The latter provides a wide-band information that can be obtained instead by a single short pulse experiment (e.g. [6]). The medium can then be reconstructed by transforming the data to the frequency domain and then using a conventional diffraction tomography reconstruction of the medium's K-space, or by modelling and processing directly in the time domain. Since the scattered fields are well localized in the spacetime domain, the time domain approach provides a transparent interpretation of the observed events and direct numerical schemes.

Physically, diffraction tomography can be explained as backpropagation of the data to the object domain. This could be performed for example using the time-domain Green function [9]. In this paper we consider a time-domain plane-wave approach that provides a rigorous setting for spectral reconstruction. A more detailed comparison between these two alternative time-domain approaches is deferred to section 5.2.

The analytic framework is the theory of the time-dependent plane-wave spectrum [10] which has been used in the past to solve various time-domain diffraction problems. The

time-dependent plane-wave spectrum is obtained from the data through the slant-stack transform (or $\tau-p$ transform, see e.g. [11, 12]), which constitutes a Radon transform in the spacetime coordinates. Thus, by formulating the time-domain scattering and inverse scattering problems in the Radon space we shall obtain a direct diffraction-tomography relation between the time-dependent plane-wave spectrum of the scattered field and the Radon transform of the medium. The major contributions of this work are thus: the time-domain Radon-space diffraction tomography mapping and its physical interpretation, the Radon space resolution and the time-domain filtered backpropagation. Note that for perfectly conducting objects, a physical-optics relation between the far-field pulsed scattering data and the objects' Radon transform has been established in [13].

Concerning the layout, the physical configuration and the conventional frequency domain formulation of diffraction tomography are briefly described in sections 2 and 3. The time-dependent plane-wave representation of the field is introduced in section 4. In the present context of diffraction tomography we consider only the 'propagating spectrum', but a complete plane-wave representation also involves the 'time-dependent evanescent spectrum'. This subject requires analytic signal representation and is not addressed here (see [10]).

The Radon space relations between the medium and the time-dependent plane-wave expansion of the scattered field are formulated in section 5. This relation also quantifies the Radon space resolution limit. Two inversion schemes are then considered in section 6: (a) A Radon-space reconstruction and (b) a time-domain filtered backpropagation. Via a numerical example in section 7 we then explore these spectral considerations and identify the sources of error (e.g. the pulse resolution and the aperture truncation).

2. Physical configuration

We are concerned with the reconstruction of an inhomogeneous dispersionless object of compact support, identified by wave-speed $v(\boldsymbol{r})$ and embedded in a uniform background with wave-speed v_0. The object is thus described by the so called 'object function'

$$O(\boldsymbol{r}) = n^2(\boldsymbol{r}) - 1 \qquad n(\boldsymbol{r}) \equiv v_0/v(\boldsymbol{r}) \tag{1}$$

where $\boldsymbol{r}$ is a position vector in a 3D coordinate space and $n(\boldsymbol{r})$ is the refractive index. The field $u(\boldsymbol{r}, t)$ satisfies the wave equation

$$[\nabla^2 - v^{-2}(\boldsymbol{r})\partial_t^2]u(\boldsymbol{r}, t) = 0. \tag{2}$$

The object is located between measurements planes at $z = z_j$, $j = 1, 2$ (figure 1) and the time-dependent scattering data there are denoted, accordingly, as $u_j(\boldsymbol{x}, t)$ where we use, conveniently, $\boldsymbol{x} = (x_1, x_2)$ for the transverse coordinates and $\boldsymbol{r} = (\boldsymbol{x}, z)$. The illumination is a time-dependent plane wave

$$u^i(\boldsymbol{r}, t) = f(t - v_0^{-1}\overset{\circ}{\boldsymbol{\kappa}}{}^i \cdot \boldsymbol{r}) \tag{3}$$

where $\overset{\circ}{\boldsymbol{\kappa}}{}^i$ is a unit vector that defines the direction of propagation and $f(t)$ is a short pulse. It will be assumed later that $\overset{\circ}{\boldsymbol{\kappa}}{}^i = \overset{\circ}{\boldsymbol{z}}$, where here and henceforth unit vectors are in bold italic and identified by a small circle over them.

3. Frequency-domain diffraction tomography

The reconstruction in this work is performed within the weak scattering Born approximation, but it can readily be extended to the Rytov model. For time-harmonic fields, these
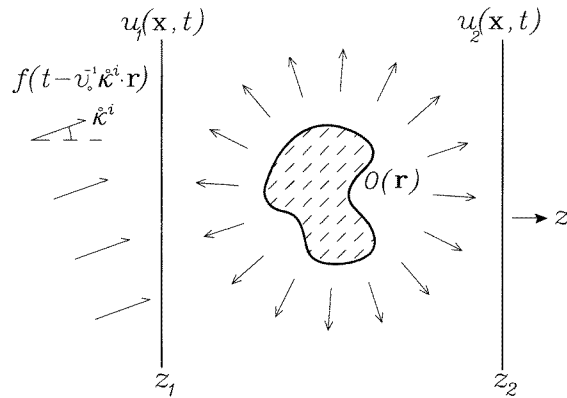
Figure 1. Physical configuration. The unknown medium is located between the measurement planes z_1 and z_2 with time-dependent data $u_1(x, t)$ and $u_2(x, t)$, respectively.

approximations reduce the object–data relation into algebraic relations in the 3D Fourier space. Our goal is to develop analogue relations directly in the time domain. We start, however, with a short review of the frequency domain relations.

Fields in the frequency domain, denoted by a circumflex, are defined by their time-domain counterparts via

$$\hat{u}(r, \omega) = \int_{-\infty}^{\infty} dt\, u(r, t)e^{i\omega t}. \tag{4}$$

Our starting point is the first Born approximation for the scattered field $\hat{u}^s$ (see [14, 15])

$$\hat{u}^s(r, \omega) = \int d^3 r'\, k^2 O(r')\hat{u}^i(r', \omega)\hat{G}(r, r'; \omega) \tag{5}$$

where $\hat{u}^i$ is the incident (unperturbed) field, $\hat{G}(r, r'; \omega) = e^{ik|r-r'|}/4\pi|r - r'|$ is the free space Green function and $k = \omega/v_0$. This approximation is valid if $O(r) \ll 1$ and if the accumulated phase-error is small [14], i.e.

$$kL(n_{\max} - 1) < \pi \tag{6}$$

where L is a typical dimension of $O(r)$ and $n_{\max}$ is a bound on $n(r)$. The validity of this condition in the time and frequency domains will be demonstrated in figures 6 and 8, respectively.

The data–object relation implied by (5), obtains a simple form in the spectral domain. With $\hat{u}_j(x, \omega)$ being the frequency-domain data on the z_j planes, the frequency-domain plane-wave spectrum of the data is defined by

$$\hat{\tilde{u}}_j(\xi, \omega) = \int d^2 x\, \hat{u}_j(x, \omega)e^{-ik\xi \cdot x} \tag{7}$$

where, anticipating extension to the time-domain, we have scaled the spectral parameter $\xi = (\xi_1, \xi_2)$ by the frequency parameter k. Consequently, ξ has a pure frequency-independent interpretation in terms of the cosines of the plane-wave angles with respect to the (x_1, x_2) axes (see (12)).

Notationally, we use a tilde to define plane-wave spectra. Thus $\hat{\tilde{}}$ denotes plane-wave spectrum in the frequency domain, obtained by the Fourier transform (7), whereas $\tilde{}$ denotes time-dependent plane-wave spectrum as obtained by the slant-stack transform (16) (see table 1).

Table 1. List of symbols.

$r = (x, z)$	3D coordinate point; $x = (x_1, x_2)$—transverse coordinates
$u(r, t)$	Time-domain field
$u_j(x, t)$	Time-dependent data on the $z = z_j$ planes, $j = 1, 2$
$\tilde{u}_j(x, \tau)$	Time-dependent plane-wave spectrum of $u_j(x, t)$ (slant-stack transform (18))
$\hat{u}(r, \omega)$	Frequency-domain field
$\hat{u}_j(x, \omega)$	Frequency-domain data
$\hat{\tilde{u}}_j(\xi, \omega)$	Frequency-domain plane-wave spectrum of $\hat{u}_j(x, t)$ (Fourier transform (7))
$\xi = (\xi_1, \xi_2)$	Spectral coordinates in (7) and (16)
$\mathring{\kappa}_j$	Direction of the scattered plane-waves in the z_j planes (12)
$u_j^b(r, t)$	Backpropagated fields (28)
$I_j(r, t)$	Imaging fields (29)
$O(r)$	The object function
$\check{O}(p, \mathring{s})$	The Radon transform of O (24)
$\bar{O}(K)$	Spatial Fourier transform of O (11)

To calculate the plane-wave spectrum of the scattered data $\hat{u}_j(x, \omega)$ we use the plane-wave expansion of $\hat{G}$ [16]

$$\hat{G}(r, r'; \omega) = \left(\frac{k}{2\pi}\right)^2 \int d^2\xi \frac{-1}{2ik\zeta} e^{ik(\xi \cdot (x - x') + \zeta|z - z'|)} \tag{8}$$

with

$$\zeta = \sqrt{1 - |\xi|^2} \qquad \text{Im}\,\zeta \geqslant 0 \tag{9}$$

where it is assumed, conveniently, that $\omega > 0$. Substituting (8) in (5) applied for $r \in z_j$ planes, using also $\hat{u}^i(r, \omega) = \hat{f}(\omega)e^{ik\mathring{\kappa}^i \cdot r}$ as implied by the incident pulse in (3) with $\hat{f}(\omega)$ being the frequency spectrum of $f(t)$, and performing the r' integration, we obtain [6, 17]

$$\hat{\tilde{u}}_j(\xi, \omega) = k^2 \hat{f}(\omega) \frac{-1}{2ik\zeta} e^{\mp ik\zeta z_j} \bar{O}(K)\Big|_{K = k(\mathring{\kappa}_j - \mathring{\kappa}^i)} \tag{10}$$

where here and henceforth upper and lower signs correspond to $j = 1$ and 2, respectively,

$$\bar{O}(K) = \int d^3r\, O(r)e^{-iK \cdot r} \qquad K = (K_{x_1}, K_{x_2}, K_z) \tag{11}$$

is the 3D Fourier transform of $O(r)$ and

$$\mathring{\kappa}_j = (\xi, \mp\zeta), \qquad |\mathring{x}_j| = 1. \tag{12}$$

The unit vectors $\mathring{\kappa}_j$ define the direction of the scattered plane-waves at the z_j planes, respectively.

Equation (10) applies for both the 'propagating' and the 'evanescent' spectral ranges ($|\xi| < 1$ and $|\xi| > 1$, respectively). In the evanescent range $\zeta = i\sqrt{|\xi|^2 - 1}$, hence (10) involves an analytic continuation of $\bar{O}$ to complex K_z. Since the evanescent-spectrum data is exponentially weak, most diffraction tomography schemes utilize only the propagating-spectrum data (see [18] for a super resolution scheme where part of the evanescent spectrum is retained). The time-dependent spectral relations developed in this work utilize, likewise, only the propagating spectrum range but they may be extended to the evanescent spectrum regime by employing the analytic signal techniques in [10].

From (10), the propagating spectrum of $\hat{u}_j$ defines $\bar{O}(K)$ only on a sphere of radius k centred at $K = -k\mathring{\kappa}^i$, henceforth referred to as the 'shifted Ewald sphere' (figure 2). A full

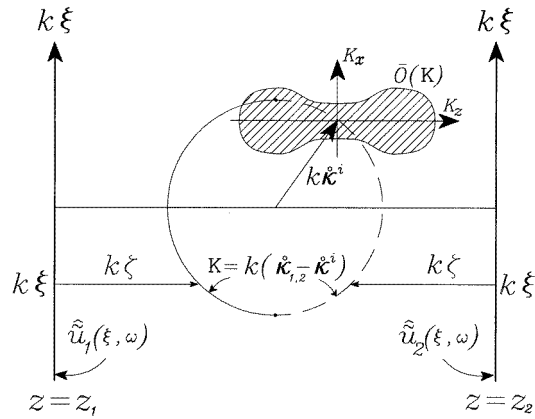**Figure 2.** The data–object relation in the K-space. The $\hat{\bar{u}}_j(\boldsymbol{\xi}, \omega)$ planes are the spectral ($\boldsymbol{\xi}$) planes of the data. $\bar{O}(K)$ (shaded) is the Fourier transform of O (11). Each data point $\boldsymbol{\xi}$ in $\hat{\bar{u}}_j$ reconstructs $\bar{O}(K)$ at point $\boldsymbol{K} = k(\mathring{\boldsymbol{\kappa}}_j - \mathring{\boldsymbol{\kappa}}^i)$ on the 'shifted Ewald sphere'. The full and broken semi-spheres correspond to data described by $\hat{\bar{u}}_{1,2}$, respectively.

K-space reconstruction of the object therefore requires additional experiments. One option is to change the illumination direction (*angular diversity*). $O(\boldsymbol{r})$ can then be found either by *spectral reconstruction* of $\bar{O}(\boldsymbol{K})$ via (10) or by *filtered backpropagation* [5, 6, 17].

An alternative approach to cover the K-space is to change the excitation frequency (*frequency diversity*). This can be done either by performing multiple monochromatic experiments or by performing a single experiment with a short excitation pulse. The data can then be analysed in the frequency domain or directly in the time domain.

Before proceeding with the time-domain analysis which is our main goal, we consider certain properties of the frequency diversity approach as implied by (10). Referring to figure 3 (where, without loss of generality, $\mathring{\boldsymbol{\kappa}}^i = \mathring{\boldsymbol{z}}$) we note that at any given frequency, the data $\hat{u}_{1,2}$ define $\bar{O}(\boldsymbol{K})$ over the left and right halves of the shifted Ewald sphere, respectively (see the full and shaded circles in figure 3). Considering the frequency band $k_{min} < k < k_{max}$ it follows that the reflection and transmission data reconstruct the horizontally and vertically shaded K-space zones in figure 3, respectively. These zones can be regarded as K-space filters for the reconstructed object. The object can then be reconstructed either by K-space reconstruction or by backpropagating the filtered time-dependent data to the object domain (see section 6 below).
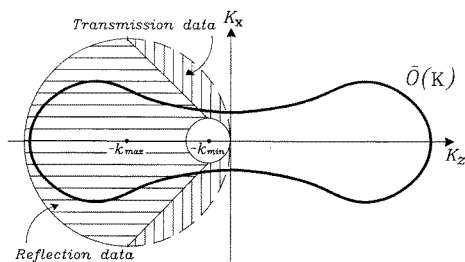

Figure 3. Frequency diversity experiment. The figure depicts the K-space regions reconstructed by $\hat{\bar{u}}_1$ and $\hat{\bar{u}}_2$.

4. Time-dependent plane-wave representation of wave fields

We briefly present here the time-dependent plane-wave representation which will be used later on in the time-domain data analysis. Let $u_0(\boldsymbol{x}, t)$ be a given field on some constant z plane, say $z = 0$ whose sources are at $z < 0$. Denoting the frequency-domain counterpart of $u_0(\boldsymbol{x}, t)$ as $\hat{u}_0(\boldsymbol{x}, \omega)$, the frequency-domain plane wave spectrum is given by (see (7))

$$\hat{\tilde{u}}_0(\boldsymbol{\xi}, \omega) = \int \mathrm{d}^2x \, \hat{u}_0(\boldsymbol{x}, \omega)\mathrm{e}^{-\mathrm{i}k\boldsymbol{\xi}\cdot\boldsymbol{x}} \tag{13}$$

and the forward propagating field is thus given by

$$\hat{u}(\boldsymbol{r}, \omega) = \left(\frac{k}{2\pi}\right)^2 \int \mathrm{d}^2\xi \, \mathrm{e}^{\mathrm{i}k(\boldsymbol{\xi}\cdot\boldsymbol{x}+\zeta z)}\hat{\tilde{u}}_0(\boldsymbol{\xi}, \omega) \tag{14}$$

where ζ is defined in (9). Equation (14) describes the field as a superposition of plane waves. In the 'propagating spectrum' range ($|\boldsymbol{\xi}| < 1$) they propagate in the directions $\overset{\circ}{\boldsymbol{\kappa}} = (\boldsymbol{\xi}, \zeta)$ (see (12)). In the 'evanescent spectrum' range $|\boldsymbol{\xi}| > 1$, $\zeta = \mathrm{i}|\zeta|$ (for $\omega > 0$) and the plane waves decay in the positive z direction.

The 'time-dependent plane-wave spectrum' $\tilde{u}_0$ may be defined from the frequency-domain plane wave spectrum via

$$\tilde{u}_0(\boldsymbol{\xi}, \tau) = \frac{1}{2\pi} \int_{-\infty}^{\infty} \mathrm{d}\omega \, \mathrm{e}^{-\mathrm{i}\omega\tau}\hat{\tilde{u}}_0(\boldsymbol{\xi}, \omega) \tag{15}$$

where the notation system is explained after (7) (see table 1).

Alternatively, $\tilde{u}_0$ may be defined directly from the time-domain data. Substituting (13) into (15), inverting the order of integrations and then evaluating the ω-integrations in closed form using (4) (this procedure is valid if $u_0(\boldsymbol{x}, t) \in \mathcal{L}^2_{\boldsymbol{x}, t}$, which is the case for scattering of a finite energy pulse $f(t)$ by a bounded, compact support $O(\boldsymbol{r})$), we obtain

$$\tilde{u}_0(\boldsymbol{\xi}, \tau) = \int \mathrm{d}^2x \, u_0(\boldsymbol{x}, \tau + v_0^{-1}\boldsymbol{\xi} \cdot \boldsymbol{x}). \tag{16}$$

This integral constitutes a Radon transform in the three-dimensional $(\boldsymbol{x}, t)$ domain, consisting of projections of the data u_0 along the slanted surfaces $t = \tau + v_0^{-1}\boldsymbol{\xi} \cdot \boldsymbol{x}$ (figure 4(a)). It is therefore termed a 'slant-stack transform'. For a given $\boldsymbol{\xi}$ it extracts time-dependent plane-wave information in the spatial direction $\overset{\circ}{\boldsymbol{\kappa}} = (\boldsymbol{\xi}, \zeta)$ (figure 4(b)). The radiated field can then be expressed as an angular superposition of these time-dependent plane waves (see (17)).

The time-dependent plane-wave representation of the radiated field is obtained by inverting (14) to the time-domain. Some special care is required when dealing with the
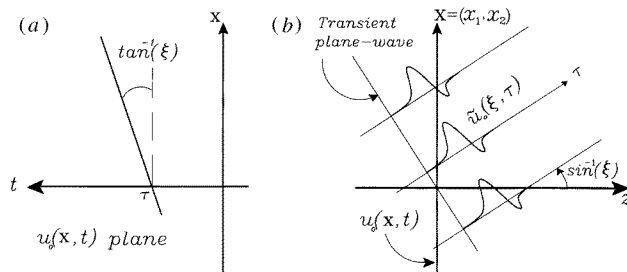

Figure 4. Transient plane-wave spectrum: (*a*) The slant stack transform of $u_0(\boldsymbol{x}, t)$ (16), (*b*) a time-dependent plane-wave representation of the field in the configuration space.

evanescent spectrum range $|\boldsymbol{\xi}| > 1$ where ζ is complex, hence this range requires an *analytic signal* plane-wave representation (see [10]). However, as discussed after (11), the evanescent spectrum is usually ignored in diffraction tomography, hence we shall consider below only the contribution of the time-dependent propagating spectrum. Thus restricting the integration domain in (14) to the spectral region $|\boldsymbol{\xi}| < 1$ and inverting the result to the time domain by following the procedure outlined in connection with (16), we obtain

$$u_{\text{prop}}(\boldsymbol{r}, t) = -(2\pi v_0)^{-2} \int_{|\boldsymbol{\xi}|<1} \mathrm{d}^2\xi \, \partial_t^2 \tilde{u}_0[\boldsymbol{\xi}, t - v_0^{-1}(\boldsymbol{\xi} \cdot \boldsymbol{x} + \zeta z)]. \tag{17}$$

Equation (17) expresses the field as an angular superposition of 'time-dependent plane waves' $\tilde{u}_0[\boldsymbol{\xi}, t - v_0^{-1}(\boldsymbol{\xi} \cdot \boldsymbol{x} + \zeta z)]$ propagating in the $\overset{\circ}{\boldsymbol{\kappa}}$ direction (figure 4(b)).

5. Data–object relation in the time-domain

Following (16), the time-dependent spectrum of the data $u_j(\boldsymbol{x}, t)$ measured on the z_j plane, $j = 1, 2$, is defined by

$$\tilde{u}_j(\boldsymbol{\xi}, \tau) = \int \mathrm{d}^2 x \, u_j(\boldsymbol{x}, \tau + v_0^{-1}\boldsymbol{\xi} \cdot \boldsymbol{x}). \tag{18}$$

$\tilde{u}_j(\boldsymbol{\xi}, \tau)$ are the time-domain counterparts of the frequency domain plane-wave spectra $\hat{\tilde{u}}_j(\boldsymbol{x}, \omega)$ in (7). They describe the scattered field as a superposition of time-dependent plane waves propagating in the direction $\overset{\circ}{\boldsymbol{\kappa}}_j$ of (12).

The time-domain relation between the data and the object will be derived next by transforming the corresponding frequency-domain relation (10) via (15). Without loss of generality we assume that $\overset{\circ}{\boldsymbol{\kappa}}^i = \overset{\circ}{\boldsymbol{z}}$. As discussed in connection with (17), we consider only the propagating spectrum $|\boldsymbol{\xi}| < 1$ but the analysis can be extended to include the time-dependent evanescent spectrum.

Substituting (10) with (11), (12) into (15) we obtain

$$\tilde{u}_j(\boldsymbol{\xi}, \tau) = \frac{1}{2\pi} \int_{-\infty}^{\infty} \mathrm{d}\omega \int \mathrm{d}^3r \, O(\boldsymbol{r}) \frac{-1}{2\mathrm{i}\zeta} k \hat{f}(\omega) \mathrm{e}^{-\mathrm{i}\omega(\tau+\tau_j)} = \frac{-1}{2\zeta v_0} \int \mathrm{d}^3r \, O(\boldsymbol{r}) f'(\tau + \tau_j) \tag{19}$$

where f' is the derivative of the excitation pulse and

$$\tau_j = [(\overset{\circ}{\boldsymbol{\kappa}}_j - \overset{\circ}{\boldsymbol{\kappa}}^i) \cdot \boldsymbol{r} \pm \zeta z_j]/v_0 \qquad \overset{\circ}{\boldsymbol{\kappa}}^i = \overset{\circ}{\boldsymbol{z}}. \tag{20}$$

To clarify this expression we introduce new spectral variables $(\overset{\circ}{\boldsymbol{s}}_j, p_j)$ instead of $(\boldsymbol{\xi}, \tau)$. For $j = 1, 2$, $\overset{\circ}{\boldsymbol{s}}_j$ are unit vectors with spherical angles $(\theta_{s_j}, \phi_{s_j})$, where θ_{s_j} is measured with respect to the *negative z*-axis. For a given $\boldsymbol{\xi}$, $\overset{\circ}{\boldsymbol{s}}_j$ are defined by

$$\theta_{s_j} = (\pi - \theta_j)/2 \qquad \phi_{s_j} = \phi_j \tag{21}$$

where (θ_j, ϕ_j) are the spherical angles of the propagation vectors $\overset{\circ}{\boldsymbol{\kappa}}_j(\boldsymbol{\xi})$ of (12). Thus $\overset{\circ}{\boldsymbol{s}}_j$ bisect the angles between the incident wave direction and the scattered plane wave directions $\overset{\circ}{\boldsymbol{\kappa}}_j$ (see figure 5). Since $\overset{\circ}{\boldsymbol{\kappa}}^i = \overset{\circ}{\boldsymbol{z}}$ here, we find that

$$\overset{\circ}{\boldsymbol{s}}_j = (\overset{\circ}{\boldsymbol{\kappa}}_j - \overset{\circ}{\boldsymbol{\kappa}}^i)/2\cos\theta_{s_j} \qquad \overset{\circ}{\boldsymbol{\kappa}}^i = \overset{\circ}{\boldsymbol{z}}. \tag{22}$$

Next, instead of τ we introduce

$$p_j = \frac{-1}{2\cos\theta_{s_j}}(v_0\tau + z_j \cos 2\theta_{s_j}). \tag{23}$$
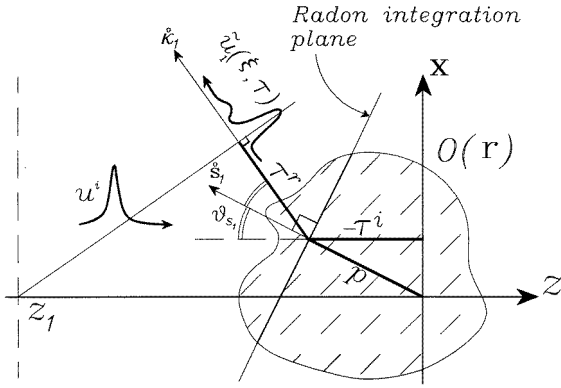
Figure 5. Time-domain data–object relation (Radon transform mapping). The figure shows the incident pulsed plane-wave u^i and one scattered time-dependent plane wave $\tilde{u}(\xi, \tau)$ in the $\overset{\circ}{\kappa}_1$ direction (the figure considers $\tilde{u}_1$ only). This scattered plane wave is described in (24) by specular 'plane wave reflections' due to the Radon transform $\check{O}(p, \overset{\circ}{s})$ of O where the axis $\overset{\circ}{s}$ bisects the angle between the directions of incidence and scattering ($\overset{\circ}{\kappa}_1$), while the distance p determines the spectral arrival time τ (see the Radon variables mapping in (21) and (23)).

The interpretation of $\overset{\circ}{s}_j$ and of p_j as the Radon direction and distance variables will be discussed after (24).

Using these new variables, we obtain in equation (19) $f'(\tau + \tau_j) = f'[-2v_0^{-1} \cos\theta_s (p - \overset{\circ}{s} \cdot r)]|_{p=p_j, \overset{\circ}{s}=\overset{\circ}{s}_j}$, so that equation (19) can be rewritten as

$$\tilde{u}_j(\xi, \tau) = f(-2v_0^{-1}\cos\theta_s p) \overset{p}{\otimes} \frac{\partial_p}{4\zeta\cos\theta_s} \int d^3r\, O(r)\delta(p - \overset{\circ}{s} \cdot r)\Big|_{p=p_j, \overset{\circ}{s}=\overset{\circ}{s}_j}$$

$$= f(-2v_0^{-1}\cos\theta_s p) \overset{p}{\otimes} \frac{\partial_p}{4\zeta\cos\theta_s} \check{O}(p, \overset{\circ}{s})\Big|_{p=p_j, \overset{\circ}{s}=\overset{\circ}{s}_j} \tag{24}$$

where $\overset{p}{\otimes}$ denotes a convolution with respect to the geometrical coordinate p. Here $\check{O}(p, \overset{\circ}{s})$ is the Radon transform of the object function, consisting of projections of O along planes normal to $\overset{\circ}{s}$ at a distance p from the origin.

Equation (24) (or its approximate form (26) below) is the main result in this section. It expresses the time-dependent plane-wave field $\tilde{u}_j(\xi, \tau)$ in the direction $\overset{\circ}{\kappa}_j$ in terms of the projections of O along planes normal to $\overset{\circ}{s}_j$. The location of p_j of these plane along the $\overset{\circ}{s}_j$ axis is determined by the spectral time τ via (23). Note that $\tilde{u}_{1,2}$ are related to projections in the spectral ranges $\theta_{s_1} \in (0, \frac{\pi}{4})$, and $\theta_{s_2} \in (\frac{\pi}{4}, \frac{\pi}{2})$, respectively. Furthermore, due to the scaling $v_0\, d\tau = -2\cos\theta_{s_j}\, dp$ implied by (23), $\check{O}(p, \overset{\circ}{s})$ at a given direction $\overset{\circ}{s}$ is compressed by an angle dependent factor $2v_0^{-1}\cos\theta_{s_j}$ when transformed to the time-dependent data $\tilde{u}_j$ via (24). The physical interpretation of these relations will be discussed below.

5.1. Spectral resolution

Assuming next that the excitation $f(t)$ is a short pulse of length T, it follows that the p-convolution in (24) resolves details in $\check{O}(p, \overset{\circ}{s})$ of the order

$$\Delta_p(\overset{\circ}{s}) \simeq v_0 T/2 \cos\theta_s. \tag{25}$$

Recalling (21), the best resolution of $\check{O}(p, \overset{\circ}{s})$ is obtained for $\tilde{u}_1$ with small $|\boldsymbol{\xi}|$ and the worst is obtained for $\tilde{u}_2$ as $|\boldsymbol{\xi}| \rightarrow 0$ (where $\theta_s \rightarrow \frac{1}{2}\pi$).

For directions $\overset{\circ}{s}$ at which $\Delta_p(\overset{\circ}{s})$ is much smaller than the details in $\check{O}(p, \overset{\circ}{s})$, the pulse $f(t)$ in (24) may be replaced by $\delta(t)$, giving

$$\tilde{u}_j(\boldsymbol{\xi}, \tau) \simeq \frac{v_0}{8\zeta \cos^2 \theta_s} \partial_p \check{O}(p, \overset{\circ}{s})\bigg|_{p=p_j, \overset{\circ}{s}=\overset{\circ}{s}_j}. \tag{26}$$

Condition (25) can be derived from frequency-domain considerations by referring to figure 3. In view of (22), the shifted Ewald sphere constraint $\boldsymbol{K} = k(\overset{\circ}{\boldsymbol{\kappa}}_j - \overset{\circ}{\boldsymbol{\kappa}}^i)$ in (10) can be expressed as $\boldsymbol{K} = \overset{\circ}{s}2k \cos \theta_s$. Thus, changing k for a given $\boldsymbol{\xi}$ describes a K-domain line in the $\overset{\circ}{s}$ direction. Along such a line $O(\boldsymbol{K})$ is determined only in the range $|\boldsymbol{K}| < 2k_{max} \cos \theta_s$ where ω_{max} is the upper frequency in $\hat{f}(\omega)$. This defines the resolution along any K-space direction $\overset{\circ}{s}$. Replacing $|\boldsymbol{K}|$ and k_{max} by $1/\Delta_p(\overset{\circ}{s})$ and $1/v_0 T$, respectively, one ends up with (25).

5.2. *Physical interpretation: pseudo plane-interface reflections*

Referring to figure 5, the planes normal to $\overset{\circ}{s}_j$ may be identified as specular reflection planes with respect to the incident plane wave that propagates in the z-direction and reflected to the $\overset{\circ}{\boldsymbol{\kappa}}_j$ direction. Thus the spectral time-dependent plane wave in the $\overset{\circ}{\boldsymbol{\kappa}}_j$ direction is generated by 'pseudo plane-interface reflections' due to the medium variations along the $\overset{\circ}{s}_j$ axis as described by the Radon transform of $O(\boldsymbol{r})$ along $\overset{\circ}{s}_j$. The location p_j of the planes along the $\overset{\circ}{s}_j$ axis is determined by the spectral observation time τ via (23). Rewriting (23) as $\tau = -2p_j \cos \theta_{s_j} - z_j \cos 2\theta_{s_j}$, τ is identified as the arrival time at the $z = z_j$ plane of the plane wave reflected from the p_j plane (the plane wave arrival time is defined as the time when the wavefront passes through the center $x = 0$ of the $z = z_j$ plane; figure 5). The reflected plane location p_j is resolved by τ only up to the incident pulselength T projected onto the reflection axis $\overset{\circ}{s}$: this explains expression (25) for the spectral resolution Δ_p.

It should be noted that a similar local reflection law has been derived asymptotically in [9]. In that paper the Born-approximated scattered field has been described by the spacetime Green function propagators along the ray from each point source to the scattering medium and thereafter to the observation points. The local reflection law has been obtained locally as a plane-surface approximation of the isochrons associated with the rays from a given source point to a given observation point (see figure 6 in [9]). In equation (27) there, this local reflection law has been expressed as a generalized Radon transform while the resolution limit of (25) has been derived there locally in figure 17 and equation (36).

Unlike the analysis in [9] which relies on local planar approximations of the ray isochron, the present relation relies on time-dependent plane waves and direct Radon transform projection of the time-dependent wave equation.

6. Inversion

We shall consider two inversion schemes: a spectral (radon-space) reconstruction and a filtered backpropagation in the configuration space.

6.1. Radon space reconstruction

Equation (24) (or (26)) relates the time-dependent plane-wave data $\tilde{u}_j(\boldsymbol{\xi}, \tau)$, obtained from the measured data $u_j(\boldsymbol{x}, t)$ via (16), to the Radon transform of O along the direction $\mathring{\boldsymbol{s}}_j$. Using the data $u_j(\boldsymbol{x}, t)$ we may therefore recover $\check{O}(p, \mathring{\boldsymbol{s}})$ in the spectral regimes $\theta_s \in (0, \frac{\pi}{4})$ and $\theta_s \in (\frac{\pi}{4}, \frac{\pi}{2})$, respectively. Taken together, they provide full coverage of the Radon space, thus $O(\boldsymbol{r})$ can be reconstructed via an inverse Radon transform [19]

$$O(\boldsymbol{r}) = \frac{-1}{4\pi^2} \int_{\Omega} \mathrm{d}^2 \mathring{\boldsymbol{s}} \, \partial_p^2 \check{O}(p, \mathring{\boldsymbol{s}}) \Big|_{p=\mathring{\boldsymbol{s}} \cdot \boldsymbol{r}} \tag{27}$$

where Ω is the half sphere $0 < \theta_s < \pi/2$.

6.2. Reconstruction via filtered backpropagation

6.2.1. Filtered backpropagation. Following (17), we define the time-dependent back-propagated fields corresponding to the data $u_j(\boldsymbol{x}, t)$ as

$$u_j^b(\boldsymbol{r}, t) = \frac{1}{2\pi} \int_{|\boldsymbol{\xi}| \leqslant 1} \mathrm{d}^2 \xi \, \tilde{u}_j[\boldsymbol{\xi}, t - v_0^{-1}(\boldsymbol{\xi} \cdot \boldsymbol{x} \mp \zeta(z - z_j))] \tag{28}$$

where $\tilde{u}_j$ are calculated from u_j via (16) and, as before, upper and lower signs correspond to $j = 1, 2$. The integral in (28) consists of time-dependent plane waves that are backpropagated from the measurement planes z_j toward the reconstruction domain. As discussed earlier, only the propagating spectral range $|\boldsymbol{\xi}| < 1$ is considered. Note that in (28) we have omitted the second order time-derivative which appears in (17) so that u_j^b calculated via (28) are, in fact, the second order time-integrals of the actual backpropagated fields.

Next we define the imaging fields $I_j(\boldsymbol{r}, t)$

$$I_j(\boldsymbol{r}, t) = 2v_0^{-1} \partial_z \{F(t + v_0^{-1}z) \overset{t}{\otimes} u_j^b(\boldsymbol{r}, t)\} \tag{29}$$

where

$$F(t) = \frac{1}{2\pi} \int_{|\omega| < \omega_{max}} \mathrm{d}\omega \, \mathrm{e}^{-\mathrm{i}\omega t} \frac{1}{\hat{f}(\omega)} \tag{30}$$

deconvolves the excitation signal $f(t)$ from the scattered signal. The Fourier inversion in (30) has been limited to the range $|\omega| < \omega_{max}$ where $\hat{f}$ is non-negligible. The maximal resolution that can be obtained in a given direction $\mathring{s}$ is therefore limited by Δ_p of (25) wherein T is replaced by ω_{max}^{-1}.

6.2.2. Reconstruction. Next we show how the backpropagated fields reconstruct $O(\boldsymbol{r})$. We start by rewriting (28), (29) in the form

$$I_j(\boldsymbol{r}, t) = F(t) \overset{t}{\otimes} \frac{\partial_z}{v_0 2\pi^2} \int_{\Omega_j} \mathrm{d}^2 \mathring{\boldsymbol{s}} \, 4\zeta \cos \theta_s \tilde{u}_j(\boldsymbol{\xi}, t - \tau_j) \tag{31}$$

where we have changed the integration variables from $\boldsymbol{\xi}$ to $\mathring{\boldsymbol{s}}$ using (22) and $\mathrm{d}^2 \xi = 4\zeta \cos \theta_s \, \mathrm{d}^2 \mathring{\boldsymbol{s}}$, Ω_j are the integration domains covered by the Radon direction vectors $\mathring{\boldsymbol{s}}_j$ (i.e. $\theta_s \in (0, \frac{\pi}{4})$ and $(\frac{\pi}{4}, \frac{\pi}{2})$, respectively), and τ_j are defined in (20).

Next we substitute the Born-approximated data–object relation (24) into (31). Noting from (23) that $p_j|_{\tau=t-\tau_j} = \overset{\circ}{s} \cdot r - \frac{1}{2}v_0 t/\cos\theta_s$ we obtain

$$I_j(r, t) = F(t) \overset{t}{\otimes} f(t) \overset{t}{\otimes} \frac{\partial_z}{2\pi^2} \int_{\Omega_j} d^2\overset{\circ}{s} \frac{\partial_p}{2\cos\theta_s} \check{O}(p, \overset{\circ}{s}) \Bigg|_{p=\overset{\circ}{s}\cdot r - v_0 t/2\cos\theta_s}. \tag{32}$$

In view of (30) we note that

$$F(t) \overset{t}{\otimes} f(t) = \delta_T(t) \equiv \frac{1}{\pi T} \frac{\sin t/T}{t/T} \qquad T = \omega_{max}^{-1} \tag{33}$$

where δ_T is the 'band limited δ function'. Introducing $\delta_T(t) \overset{t}{\otimes}$ into the integral and replacing it by $\delta_{\Delta_p}(p) \overset{p}{\otimes}$, where $\Delta_p(\overset{\circ}{s})$ is defined in (25), using also $\partial_p = \cos\theta_s\partial_z$, equation (32) becomes

$$I_j(r, t) = \frac{-1}{4\pi^2} \int_{\Omega_j} d^2\overset{\circ}{s} \, \partial_p^2 \delta_{\Delta_p}(p) \overset{p}{\otimes} \check{O}(p, \overset{\circ}{s}) \Bigg|_{p=\overset{\circ}{s}\cdot r - v_0 t/2\cos\theta_s}. \tag{34}$$

$\check{O}^{(T)}(p, \overset{\circ}{s}) = \delta_{\Delta_p}(p) \overset{p}{\otimes} \check{O}(p, \overset{\circ}{s})$ will be denoted the 'limited spectrum Radon transform' of O.

Next we impose the so-called *imaging condition* $t = 0$ (see interpretation below) and obtain

$$I_1(r, 0) + I_2(r, 0) = \frac{-1}{4\pi^2} \int_{\Omega} d^2\overset{\circ}{s} \, \partial_p^2 \check{O}^{(T)}(p, \overset{\circ}{s}) \Bigg|_{p=\overset{\circ}{s}\cdot r}. \tag{35}$$

where $\Omega = \Omega_1 + \Omega_2$ is the half sphere $0 < \theta_s < \pi/2$. Identifying (35) as an inverse Radon transform (27) we obtain the reconstruction formula

$$O^{(T)}(r) = I_1(r, 0) + I_2(r, 0). \tag{36}$$

Thus $O_j^{(T)}(r) \equiv I_j(r, 0)$ are the limited spectrum partial images due to data on the z_j planes. In view of (34), these partial images correspond to the spectral regions Ω_j in the Radon domain.

For a given image point r, the imaging condition $t = 0$ defines the trajectories $\tau(\xi, r) = -\tau_j = -v_0^{-1}[\xi \cdot x \mp \zeta(z - z_j) - z]$ in the (ξ, τ) plane, along which the data in (31) is integrated (typical trajectories are plotted in figure 13). The interpretation of this condition thus follows at once by noting that τ_j of (20) is the arrival time at the measurement plane z_j of the scattered pulsed plane wave excited as the incident pulse passes through r (see (20)).

Finally, the definition of I_j in (29) includes a convolution of h_j^b with F which deconvolves the excitation signal f from the data. If, however, f is short enough then this convolution can be ignored. The reconstructed $O_j^{(T)}$ in (36) are thus given directly in terms of the backpropagated fields h_j^b,

$$O_j^{(T)}(r) = I_j(r, 0) \simeq 2v_0^{-1}\partial_z h_j^b(r, t)|_{t=z/v_0}. \tag{37}$$

6.2.3. A summary of the time-domain filtered backpropagation algorithm. In view of the above analysis, the reconstruction procedure is as follows:

(1) Calculate $\tilde{u}_j(\xi, \tau)$ from the data $u_j(x, t)$ via (18).

(2) Calculate the backpropagated fields $u_j^b(r, t)$ via (28), and then the image fields $I_j(r, t)$ via (29) or (37) (for the filtered or the unfiltered backpropagation, respectively).

(3) Identify the partial images $O_j^{(T)}(r) = I_j(r, 0)$ via (36) or (37).

7. Numerical example: a homogeneous sphere

We consider a homogeneous sphere with refractive index n_0 and radius $a = 1$. The background wave speed is $v_0 = 1$. The boundary conditions are the continuity of the field and its normal derivative. The sphere is centred at the coordinates origin and the measurement planes are $z_{1,2} = \mp 2$. The incident pulse in (3) was taken to be a Gaussian,

$$f(t) = (\pi T)^{-1/2} e^{-(t/T)^2} \longleftrightarrow \hat{f}(\omega) = e^{-(T\omega/2)^2}. \tag{38}$$

We choose $T = \frac{1}{8}$ which justifies the approximation of $f(t)$ by $\delta(t)$ in (24), and thus the approximate reconstruction (37).

7.1. The scattering data

The exact time-harmonic field has been calculated via a Mie series and then transformed into the time-domain. These exact time-harmonic and time-dependent fields have been compared with the Born approximation. Figure 6 compares the exact and the Born solutions as a function of ka for $n_0 = 1.1$. The observation points are on the symmetry (z) axis at $z_{1,2}$. The Born solution is seen to be valid for $ka < 15$ as implied by (6). Note, however, the relatively large phase error of the Born solution for $\hat{u}_1$ in that frequency range. This error is due to interference with internal reflections, and is thus absent in the time domain signal prior to the arrival of these reflections. This is one advantage of the time-domain inversion which employs the early time signal.

The exact time-domain signals $u_{1,2}(x, t)$ at various points x in the measurement planes are shown in figure 7, and then compared with the Born results in figure 8. Note that the Born solution does not describe the late-time internal reflections in u_1. This explains the phase inaccuracy observed in figure 6. For u_2, the contribution of the internal reflections is weaker since they arrive after two internal reflections, one from the back face followed by one from the front face.

7.2. Spectral processing and reconstruction

The reconstruction consists of two stages: calculation of $\tilde{u}_j(\xi, \tau)$ and then backpropagation.

7.2.1. Calculation of $\tilde{u}_j(\xi, \tau)$. The time-dependent plane-wave spectra $\tilde{u}_j(\xi, \tau)$, calculated from the exact data $u_{1,2}(x, t)$ in figure 7 via (16), are depicted in figure 9 for values of $\xi_\rho = \sqrt{\xi_{x_1}^2 + \xi_{x_2}^2}$ between 0 and 1. The aperture data used for the procesing was taken for $\rho = \sqrt{x_1^2 + x_2^2} < 10$. This limited aperture effect is observed along a diagonal extending
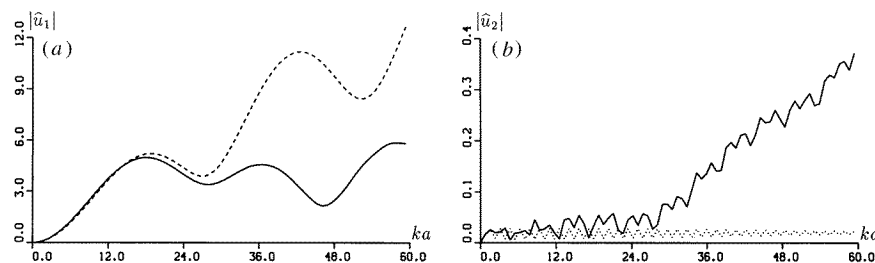

Figure 6. The exact (full curve) and the Born (broken curve) solutions as a function of ka for a sphere with $n_0 = 1.1$: (*a*) $\hat{u}_1$, (*b*) $\hat{u}_2$.
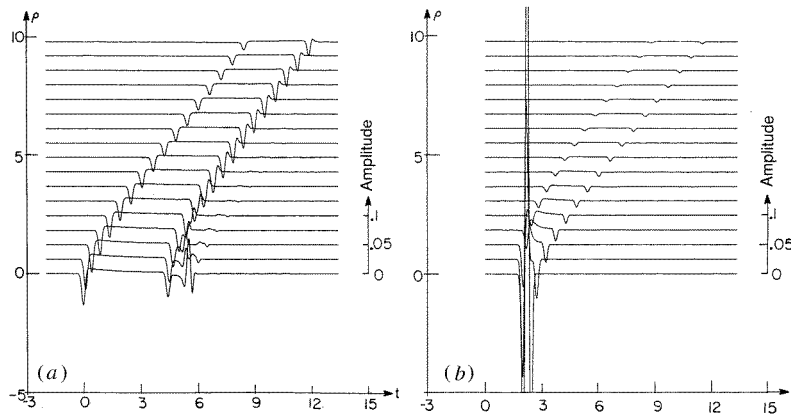
Figure 7. The exact time-dependent data calculated at various points $\rho = \sqrt{x^2 + y^2}$ in the measurement planes: (a) $u_1(x, t)$, (b) $u_2(x, t)$.
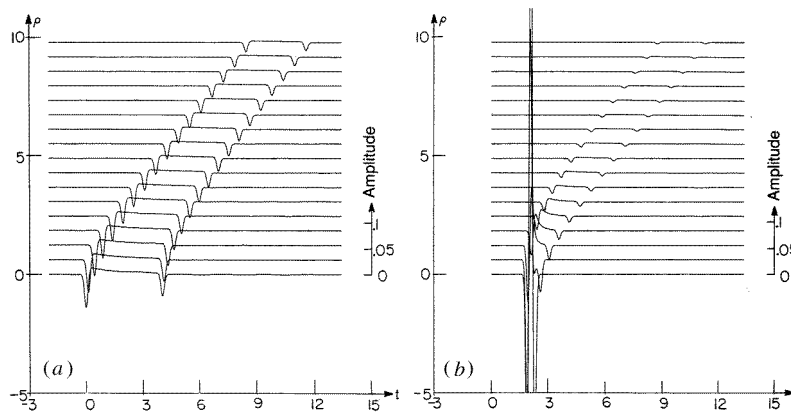

Figure 8. As in figure 7 but for the Born-approximated field.

from $(\tau, \xi_\rho) \simeq (9, 0)$ to $(\tau, \xi_\rho) \simeq (3, 1)$. Thus, it is within the *object domain* only for large ξ_ρ. The effect of this error on the reconstruction will be discussed in the next section. Note also that the contribution of the internal reflections in $\tilde{u}_1$ (figure 9(a)) is confined essentially in the range $4 < \tau < 6$ for small ξ_ρ, outside the *object domain*. For u_2 (figure 9(b)), the internal reflections are hardly observed (see discussion in section 7.1).

In order to understand the results in figure 9, we show in figure 10 the synthetic Born-approximated spectra $\tilde{u}_j(\xi, \tau)$ as calculated via (24) from the Radon transform of $O(r)$. The Radon transform of the spherical scatterer is given by $\check{O}(p, \overset{\circ}{s}) = \pi(n_0^2 - 1)(1 - p^2)H(1 - |p|)$, hence, from (24), the synthetic Born spectrum is

$$\tilde{u}_j(\xi_\rho, \tau) = f(\tau) \overset{\tau}{\otimes} \pi(n_0^2 - 1)\frac{(\tau \pm z_j\zeta)H(\sqrt{2(1 \pm \zeta)} - |\tau \pm z_j\zeta|)}{\sqrt{8}\zeta(1 \pm \zeta)^{\frac{3}{2}}} \tag{39}$$

where $\zeta = \sqrt{1 - \xi_\rho^2}$. This result is shown in figure 10. Note the angle-dependent compression of the Radon transform when transformed to $\tilde{u}_j$ as implied by the scaling $v_0 \, \mathrm{d}\tau = -2\cos\theta_s \, \mathrm{d}p$. (Indeed the waveforms become shorter and stronger as ξ_ρ changes from 0 to 1 for u_1 and from 1 to 0 for u_2.) This causes a loss of resolution in the forward

direction (i.e. in $\tilde{u}_2$ with small ξ_ρ) when the synthetic Radon transform pulse is convolved with $f(\tau)$, and the pulse-shape there is determined essentially by $f(t)$. The effect of this finite resolution will be considered in the next section.

7.2.2. Reconstruction. The reconstructed function O has been calculated via (36), (37). Figure 11 depicts cross sectional cuts of O at various distances ρ from the symmetry axis. The figure shows the individual contributions of the u_1 and u_2 data (i.e. $O_{1,2}$) as well as the combined result. u_1 provides good axial resolution (see (25) for small θ_s) while u_2 provides the axial *average* information and poor lateral resolution. The quality of the combined reconstruction can be assessed from figures 11 and 12.

   The main sources of error are the limited aperture of the data u_j which affects $\tilde{u}_j$, and the finite reclusion of the pulse (see section 7.2.1). The latter affects, essentially, the lateral resolution of O_2 in figure 11. To track the effect of the limited aperture we superimpose the imaging trajectories $\tau(\boldsymbol{\xi}, \boldsymbol{r})$ in figure 13 on the $\tilde{u}_{1,2}$ plane in figure 9. These trajectories are plotted in figure 13 for several image points on the z-axis. As noted after (36), the reconstructed O at a given $\boldsymbol{r}$ is obtained by integrating $\tilde{u}_{1,2}$ along these trajectories. One
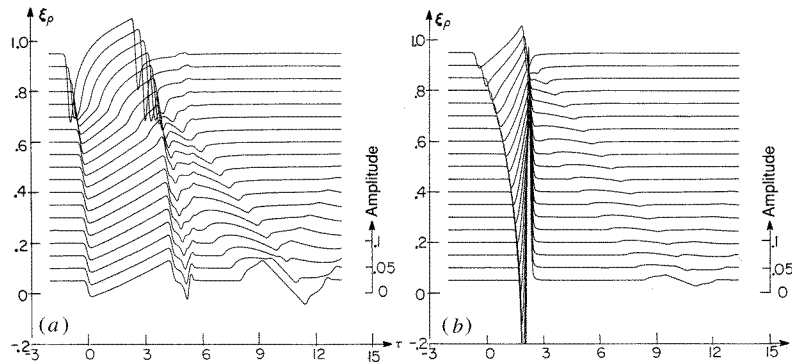

Figure 9. Time-dependent plane-wave spectrum of the exact data in figure 7, shown for $1 < \xi_\rho < 1$: (*a*) $\tilde{u}_1(\boldsymbol{\xi}, \tau)$, (*b*) $\tilde{u}_2(\boldsymbol{\xi}, \tau)$. Note the scale difference in the amplitude for $\tilde{u}_1$ and $\tilde{u}_2$.
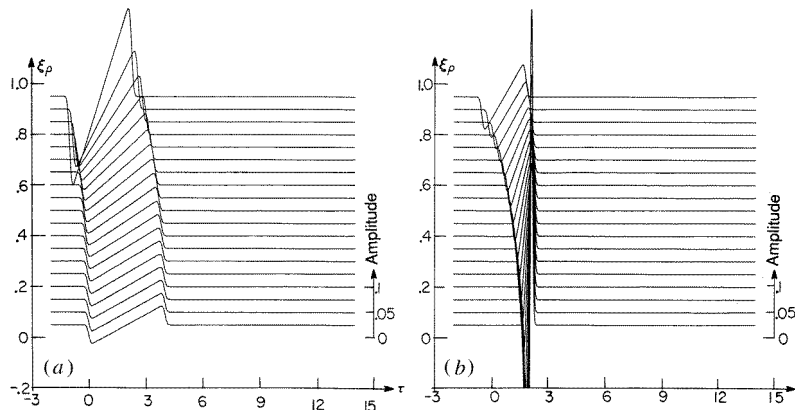

Figure 10. Synthetic time-dependent plane-wave spectrum under the Born approximation, calculated from (39). The figure format is the same as in figure 9.
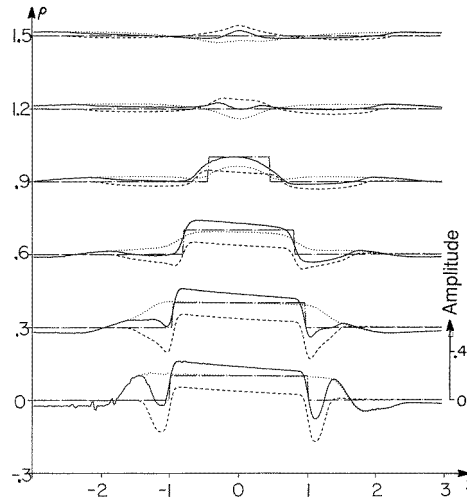
Figure 11. Cross sectional cuts of the reconstructed $O(r)$ at various distances ρ from the symmetry axis. Chain curves: the original scatterer with $n_0 = 1.1$. Broken and dotted curves: reconstruction with reflection and with transmission data only (i.e. reconstruction of $O_{1,2}$, respectively). Full curves: full reconstruction (i.e. $O_1 + O_2$).
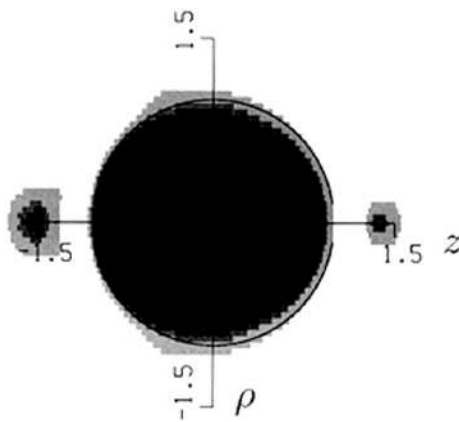

Figure 12. Grey representation of the reconstruction in figure 11 for $n_0 = 1.1$. Black: 10% error, dark grey: 25% error, light grey: 60% error.
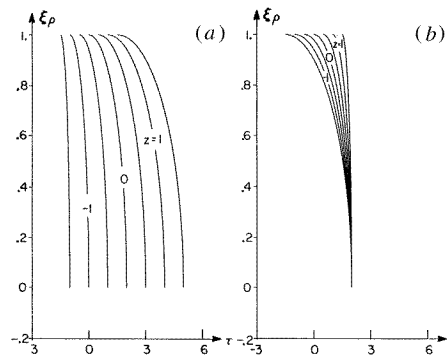
Figure 13. Imaging integration trajectories (see discussion after (36)) plotted in the (ξ_ρ, τ) domain of $\tilde{u}_{1,2}$ (see figure 9). The curves correspond to image points on the z axis at $z = 0, \pm 0.5, \pm 1, \pm 1.5$.

finds that the two ghost images at $z \simeq \pm 1.2$ are essentially due to the error in $\tilde{u}_{1,2}$ at large ξ_ρ values in figure 9, which has been identified in section 7.2.1 as truncated aperture error. Finally, as discussed in connection with figure 9, the effect of internal reflections which are not included in the Born model is minor for the present set of parameters.

8. Summary and conclusions

We presented a time-domain diffraction tomography using a spectral theory of time-dependent plane waves. The analytical framework is structured about the Radon transform:

as has been shown in (24), the time-dependent plane-waves spectrum $\tilde{u}_j(\boldsymbol{\xi}, \tau)$, calculated from the data $u_j(\boldsymbol{x}, t)$ via the slant-stack transform (16) is *directly related* to the Radon transform of the medium $\check{O}(p, \overset{\circ}{s})$. The Radon axis $\overset{\circ}{s}$ bisects the angle between the plane-wave direction $\overset{\circ}{\boldsymbol{\kappa}}_j(\boldsymbol{\xi})$ and the incident wave, while the location p along this axis is related to the spectral observation time τ via (23). Physically, this relation describes the scattered field in any spectral direction $\overset{\circ}{\boldsymbol{\kappa}}_j$ as specular plane-interface reflections by the Radon transform of O along the $\overset{\circ}{s}$ axis (see discussion in section 5.2 and figure 5). This interpretation also clarifies the resolution limit Δ_p in (25). As noted in section 5.1, the best resolution is obtained for the axial directions, which are obtained from the reflected field, but it deteriorates in the cross-range directions which are described by the transmitted field.

Two inversion schemes have then been considered in section 6: a Radon space reconstruction (section 6.1) and a time-domain filtered backpropagation (see summary in section 6.2.3). The Radon space formulation has identified the main sources of error to be: (a) the deterioration of the pulse resolution in the forward u_2 direction, that affects the data in the cross-range Radon directions (see (25)) and (b) the aperture truncation which affects, essentially, the axial resolution. These theoretical considerations have been established through the detailed numerical example in section 7, where the emphasis has been placed on identifying the isolated effects of all sources of error.

In subsequent publications, the spectral relations developed here will be extended to a *local theory* wherein *collimated wavepackets* (pulsed beams), rather than time-dependent plane-waves, are being used as basis elements for local reconstruction.

Acknowledgments

References

[1] Tijhuis A G 1987 *Electromagnetic Inverse Profiling* (Utrecht: VNU Science) ch 5–6
[2] Chew W C and Wang Y M 1990 Reconstruction of two-dimensional permittivity distribution using the distorted Born iterative method *IEEE Trans. Med. Imag.* **9** 218–25
[3] Kleinman R E and van der Berg O M 1992 A modified gradient method for two-dimensional problems in tomography *J. Comput. Appl. Math.* **42** 17–35
[4] Devaney A J 1982 A filtered backpropagation algorithm for diffraction tomography *Ultrason. Imag.* **4** 336–49
[5] Pan S X and Kak A C 1983 A computational study of reconstruction algorithms for diffraction tomography: interpolation versus filtered backpropagation *IEEE Trans. Acoust., Speech, Signal Processing* **ASSP-31** 1262–75
[6] Langenberg K J 1987 Applied inverse problems for acoustic, electromagnetic and elastic wave scattering *Basic Methods of Tomography and Inverse Problems, Malvern Physics Series* ed P C Sabatier (Bristol: Adam Hilger)
[7] Tabbara W, Duchene B, Pichot Ch, Lesselier D, Chommelous L and Joachimowicz N 1988 Diffraction tomography: contribution to the analysis of some applications in microwaves and ultrasonics *Inverse Problems* **4** 305–31
[8] Ladas K T and Devaney A J 1991 Generalized ART algorithm for diffraction tomography *Inverse Problems* **7** 109–25
[9] Miller D, Orstaglio M and Beylkin G 1987 A new slant on seismic imaging: Migration and integral geometry *Geophysics* **52** 943–64

[10] Heyman E and Felsen L B 1987 Weakly dispersive spectral theory of transients (STT), part I: formulation and interpretation; part II: evaluation of the spectral integral; part III: applications *IEEE Trans. Antennas Propagat.* **AP-35** 80–6, 574–80, 1258–66

[11] Kappus M E, Harding A J and Orcutt J A 1990 A comparison of tau–p transform methods *Geophysics* **9** 1202–15

[12] McMechan C A and Ottolini R 1982 Direct observation of a $\tau-p$ curve in a slant staked wave field *Bull. Seism. Soc. Am.* **70** 775–89

[13] Boerner W M, Ho C M and Foo B Y 1981 Use of Radon's projection theory in electromagnetic inverse scattering *IEEE Trans. Antennas Propagat.* **AP-29** 336–41

[14] Keller J B 1969 Accuracy and validity of the Born and Rytov approximations *J. Opt. Soc. Am.* **59** 1003–4

[15] De-Hoop A T 1985 Time domain far-field scattering of plane scalar waves in the Born approximation *J. Opt. Soc. Am.* **2** 1961–4

[16] Felsen L B and Marcuvitz N 1973 *Radiation and Scattering of Waves* (Englewood Cliffs, NJ: Prentice-Hall)

[17] Devaney A J 1985 Diffraction tomography *Inverse Methods in Electromagnetic Imaging, Part 2* ed W M Boerner *et al* (Dordrecht: Reidel) pp 1107–35

[18] Schatzberg A and Devaney A J 1992 Super-resolution in diffraction tomography *Inverse Problems* **8** 149–64

[19] Dean S R 1983 *The Radon Transform and Some of Its Applications* (New York: Wiley–Interscience)